Journal of
Synchrotron
Radiation

ISSN 0909-0495

Received 11 March 2008
Accepted 28 July 2008

Image contrast in X-ray reflection interface microscopy: comparison of data with model calculations and simulations

P. Fenter,[a]* C. Park,[a] V. Kohli[a] and Z. Zhang[b]

[a]Chemical Sciences and Engineering Division, Argonne National Laboratory, Argonne, IL 60439, USA, and [b]X-ray Science Division, Argonne National Laboratory, Argonne, IL 60439, USA. E-mail: fenter@anl.gov

The contrast mechanism for imaging molecular-scale features on solid surfaces is described for X-ray reflection interface microscopy (XRIM) through comparison of experimental images with model calculations and simulated measurements. Images of elementary steps show that image contrast is controlled by changes in the incident angle of the X-ray beam with respect to the sample surface. Systematic changes in the magnitude and sign of image contrast are asymmetric for angular deviations of the sample from the specular reflection condition. No changes in image contrast are observed when defocusing the condenser or objective lenses. These data are explained with model structure-factor calculations that reproduce all of the qualitative features observed in the experimental data. These results provide new insights into the image contrast mechanism, including contrast reversal as a function of incident angle, the sensitivity of image contrast to step direction (*i.e.* up *versus* down), and the ability to maximize image contrast at almost any scattering condition defined by the vertical momentum transfer, Q_z. The full surface topography can then, in principle, be recovered by a series of images as a function of incident angle at fixed momentum transfer. Inclusion of relevant experimental details shows that the image contrast magnitude is controlled by the intersection of the reciprocal-space resolution function (*i.e.* controlled by numerical aperture of the condenser and objective lenses) and the spatially resolved interfacial structure factor of the object being imaged. Together these factors reduce the nominal contrast for a step near the specular reflection condition to a value similar to that observed experimentally. This formalism demonstrates that the XRIM images derive from limited aperture contrast, and explains how non-zero image contrast can be obtained when imaging a pure phase object corresponding to the interfacial topography.

Keywords: X-ray microscopy; X-ray reflectivity; interfacial X-ray scattering; phase contrast; full-field imaging; surface topography; structure factor; pure phase object.

1. Introduction

The ability to probe interfaces directly in complex environments has been one of the greatest strengths of interfacial X-ray scattering techniques (Feidenhans'l, 1989; Robinson, 1991; Robinson & Tweet, 1992). These approaches, which became practical only with the advent of hard X-ray synchrotron sources, have become increasingly powerful with the advent of third-generation synchrotron sources having higher brilliance, more tunability, larger flux and greater stability. To date, this set of approaches has been successful in understanding a broad range of interfacial structures, reconstructions, and processes, in a diverse range of environments (Als-Nielsen, 1987; Toney *et al.*, 1987; Braslau *et al.*, 1988; Vlieg *et al.*, 1988; Feidenhans'l, 1989; Ocko *et al.*, 1990; Robinson, 1991; Robinson & Tweet, 1992; Fenter, 2002), with excellent temporal resolution (Eres *et al.*, 2002) and elemental/chemical sensitivity (Walker *et al.*, 1991; Chu *et al.*, 1999; Park *et al.*, 2006) and even phase sensitivity (Lyman *et al.*, 2005). A largely unexplored frontier in this area is the extension of these techniques beyond spatially averaged measurements to image structures in direct space.

X-ray microscopy has used a number of distinct measurement geometries. Coherent X-ray diffraction utilizes a coherent X-ray beam that illuminates a sample (*e.g.* a nanoparticle) and records the diffraction pattern in the far field,

either using the forward scattered beam (Miao *et al.*, 1999; Shapiro *et al.*, 2005) or Bragg diffraction from the internal structure of nanoparticles (Robinson *et al.*, 2001; Williams *et al.*, 2003). These data can be inverted with the use of phasing algorithms to reveal images of the individual nanoparticles in direct space (Gerchberg & Saxton, 1972; Fienup, 1978; Sayre *et al.*, 1998; Miao *et al.*, 1999). Images of interfacial topography have also been achieved (Vartanyants *et al.*, 1997). A second class of measurements uses holographic imaging approaches to obtain real-space images of samples (Kirz *et al.*, 1992; McNulty *et al.*, 1992; Eisebitt *et al.*, 2004). A third class of measurements obtains images of materials in a microprobe mode, where a small beam is rastered across the sample while collecting a secondary signal (transmission, fluorescence, diffraction) that is plotted as a function of beam position (Manceau *et al.*, 2002; Do *et al.*, 2004). These techniques typically are not intrinsically surface sensitive since they use signals derived from the interaction of the X-rays with the sample as a whole (*e.g.* absorption, diffraction, fluorescence *etc*.). While advances in X-ray optics continue (Kang *et al.*, 2006), the ability to resolve individual atoms directly is unlikely in the foreseeable future.

Interfacial electron microscopy has been developed over the past 40 years. Since seminal work by Bauer in the development of low-energy electron microscopy (LEEM) (Bauer, 1994), many related techniques have been established including reflection high-energy electron microscopy, surface-sensitive transmission electron microscopy (Ross & Gibson, 1992; Chen & Gibson, 1998; Chiaramonti & Marks, 2005), photoemission electron microscopy (Rotermund *et al.*, 1991) and related techniques. Common to all these techniques is their ability to image molecular-scale features without molecular-scale resolution (*i.e.* while the distribution of these features can be seen, their internal structures cannot). Various contrast mechanisms have been demonstrated, including topographic sensitivity, reconstructed domains, magnet structures *etc.* (Chung & Altman, 1998; Tromp, 2000). A quantitative understanding of these mechanisms, however, suffers from the difficulty of calculating electron scattering intensities owing to the importance of multiple scattering. These approaches can only be applied to surfaces in vacuum environments.

The use of X-ray optics to image interfaces with elastically scattered X-rays, similar to approaches previously used by interfacial electron microscopy, offers a fundamentally new approach to understanding interfacial processes (Fenter *et al.*, 2006). While interfacial X-ray microscopy is likely to be challenged by limitations in source brilliance and flux, it has the potential to be used in complex environments that are otherwise inaccessible to the more mature electron-based microscopies. A key capability of X-ray microscopy is the ability, in principle, to quantify all aspects of the measured intensities, owing to the simplicity of the X-ray scattering cross section (Als-Nielsen & McMorrow, 2001).

We have recently demonstrated the feasibility of imaging interfacial topography with X-ray optics while using elastically scattered X-ray reflectivity signals (Fenter *et al.*, 2006). The use of phase contrast allowed interfacial topography to be observed, and individual features in the image could be identified as monomolecular steps having a height of 0.65 nm through measurements of interfacial contrast as a function of vertical momentum transfer in the specular reflection geometry. These results, obtained with a weak specularly reflected X-ray beam, revealed that image contrast for elementary steps is observed as destructive interference so that steps appeared as dark lines on a bright background (the latter associated with the intrinsic reflectivity of the ideally flat substrate). In one case, however, where a step was oriented transverse to the scattering plane, the image of the step appeared as adjacent bright and dark lines (Fenter *et al.*, 2006). The fact that positive contrast could be observed suggested that the image mechanism was incompletely understood and that the contrast can be manipulated experimentally. Here, we report progress in establishing the key features that control image contrast in interfacial X-ray microscopy, through experimental observations and the development of a conceptual framework for calculating and simulating images. These results show that (i) image contrast is controlled by the lateral momentum transfer as controlled by the sample orientation at fixed momentum-transfer magnitude, with both positive and negative contrast possible; (ii) the contrast can be understood through model structure-factor calculations and is controlled by the local scattering intensity of a miscut surface owing to the presence of elementary steps; (iii) the direction and height of a step (*i.e.* up or down) is revealed through observations of image contrast as a function of incident angle; (iv) inclusion of key experimental details (*i.e.* the reciprocal-space resolution volume owing to numerical aperture of the condenser and objective lenses) leads to a substantial reduction in image contrast (with respect to model calculations) that is intrinsic to the X-ray reflection interface microscopy (XRIM) configuration and is in good agreement with the experimental data. Specifically, this approach provides a first-order explanation of the image contrast magnitude as a function of incident angle without any adjustable parameters. This formalism also explains the ability of XRIM to observe non-zero contrast when imaging a pure phase object (*i.e.* phase changes owing to interfacial topography) contrary to the nominal expectation that such images would show no contrast in the absence of absorption (Paganin, 2006).

2. Experimental details

The XRIM experiment uses surface X-ray scattering (Feidenhans'l, 1989; Robinson & Tweet, 1992) in an optical configuration derived from full-field X-ray microscopy (Jacobsen *et al.*, 1991). A schematic of the experimental set-up is shown in Fig. 1. The measurements were carried out at the APS/XOR/BESSRC beamline 12-ID-D at the Advanced Photon Source at Argonne National Laboratory. The X-ray beam energy of 10.0 keV is selected using a vertical Si(111) double-bounce monochromator, and is then nominally collimated in the horizontal plane by a mirror. The monochromatic X-ray beam is incident on a condenser Fresnel zone plate

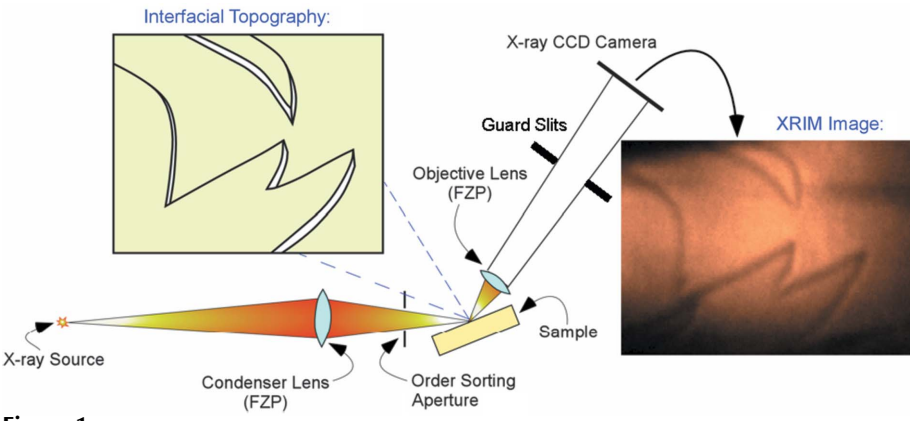

Figure 1
Schematic of the XRIM experiment showing the X-ray source and the condenser Fresnel zone plate (FZP) X-ray lens that focuses the X-ray beam to a spot on the sample having some complex surface topography. An order-sorting aperture selects the first-order diffraction condition of the FZP lens. The spatial variation of the interfacial intensity is then imaged with an objective lens onto the X-ray CCD camera. Guard slits are used between the objective FZP and the CCD camera to block any X-rays not used in the image. The intensity variation in the XRIM image (on the right) is controlled by phase contrast associated with the interfacial topography (top left).

(FZP) ∼70 m from the source. The condenser FZP has an outer diameter of 1 mm and collects ∼30% of the monochromatic undulator X-ray beam (owing to the ∼1 mm × 3 mm beam cross section). The first-order beam from the FZP is selected using an order-sorting aperture consisting of a 200 µm-diameter fixed circular aperture constructed of 0.1 mm-thick PtIr alloy located ∼40 mm upstream from the sample position. The condenser FZP has an outer zone width of 100 nm [*i.e.* the width of its outer-most ring (Attwood, 1999)] and focuses the X-ray beam with a nominal focal length of 807 mm. In the context of the interfacial scattering, the outer zone width corresponds to the transverse coherence length of the incident beam. The FZP is mounted on a three-axis motorized translation stage so that the focal point of the beam can be adjusted with respect to the sample position in three orthogonal directions. The beam size at the FZP focus corresponds to an image of the synchrotron source (modified by the upstream horizontal beamline mirror), resulting in an observed illuminated region of ∼3.5 µm × 7.2 µm in the vertical and horizontal directions transverse to the incident beam direction.

The X-ray beam is specularly reflected from the sample and the sample orientation is controlled using a four-circle diffractometer. The reflected beam is collected by the objective FZP with an outer diameter of 80 µm and an outer zone width of 50 nm, located 34 mm downstream from the sample position. An image of the spatial variation of the local interfacial scattering intensity across the surface is projected onto the CCD camera using an objective FZP, as described previously. The efficiency of the objective FZP is ∼10% with a large fraction of the reflected beam transmitted unfocused through the objective zone plate. An integrated central beam stop (∼400 µm outer diameter) in the condenser FZP and a vertical wire just before the FZP (not shown in Fig. 1) leads to a reflected beam shape in the form of a 'split ring' projected onto the CCD camera. This reflected beam profile is observed on the CCD owing to the portion of the reflected beam that is transmitted through the objective lens unfocused, but creates a dark region on the CCD camera in which the interfacial image is projected. The location of the reflected beam on the CCD camera allows the incident angle to be determined precisely. Additional guard slits between the objective lens and CCD camera block this unfocused portion of the reflected beam before it reaches the CCD camera to minimize background signals. The XRIM images are normally obtained within the central region of the transmitted beam profile to minimize background signals.

The field of view of the objective FZP is larger than that illuminated with a fixed incident beam. Consequently interfacial images are obtained by scanning the incident beam to illuminate a larger area of the surface and to provide a more uniform illumination. This is done by translating the condenser FZP both vertically and laterally to discrete positions while the sample, order-sorting aperture and objective lens remain fixed in position. A fast X-ray shutter is used to illuminate the sample only when the condenser FZP is stationary for a pre-selected time interval. The CCD camera continually integrates the interfacial image during this scanning procedure.

The intensity variation across individual steps in the XRIM images is quantified by converting the two-dimensional images to one-dimensional line-scans. These one-dimensional plots (intensity *versus* position) are obtained by projecting the two-dimensional image intensity within the region of interest onto the axis that is orthogonal to the step edge and binned into pseudo-pixels having the same 13 µm pixel spacing of the CCD camera.

The samples were prepared as described previously (Fenter *et al.*, 2000, 2006). Orthoclase (001) surfaces were cleaved in air and attached to a sample holder with glue. The XRIM measurements were performed with the sample in air. No changes to the surface were observed during the course of the measurements. The present measurements were made near the specular reflection condition and the results are discussed in terms of the momentum transfer, $\mathbf{Q} = \mathbf{K}_f - \mathbf{K}_i = (Q_x, Q_y, Q_z) = K\{\cos(\beta) - \cos(\alpha), \sin(\delta\chi)[\sin(\beta) + \sin(\alpha)], \cos(\delta\chi)[\sin(\beta) + \sin(\alpha)]\}$, where $K = |\mathbf{K}| = 2\pi/\lambda$, λ is the X-ray wavelength, α and β are the incident and exit angles of the X-ray beam with respect to the surface plane, respectively, and $\delta\chi$ is the transverse tilt of the sample away from the specular condition (*i.e.* out of the scattering plane). Here, the momentum transfer is expressed in the sample reference frame with the x and y axes within the surface plane and the z axis is along the surface normal direction. The scattering plane is coincident with the xz plane when $\delta\chi = 0$. It is convenient to describe the scattering condition in reciprocal lattice units, L, where $Q_z = (2\pi/d_{001})L$, where $d_{001} = 0.6495$ nm is the vertical layer spacing of

the orthoclase sample, and L = 1, 2, 3 corresponds to the substrate Bragg peaks. All images were obtained for L = 0.25, corresponding to an incident angle of $\alpha_0 = 1.37^\circ$ at the specular reflection condition, and where the nominal interfacial reflectivity is $\sim 10^{-5}$. Most images were obtained for exposure times of ~470 s in which the incident condenser FZP was moved over a 3 × 15 grid of points, with step sizes of 2 μm and 1 μm in the horizontal and vertical directions, respectively.

3. Results

3.1. Experimental control of image contrast

The main experimental results are summarized in Fig. 2. These images show the same region of an orthoclase (001) surface as a function of the incident angle and displacement of the condenser lens focus with respect to the sample. The intersection of two dark lines in the lower center of each image provides a fixed reference point for each image. The image obtained at the specular reflection condition (Fig. 2*a*) shows a series of dark, almost parallel, lines separated by uniform surface regions that appear bright. These images are similar to those reported previously (Fenter *et al.*, 2006) and the features are identified as elementary steps on the orthoclase surface. Images were obtained for two different positions of the condenser FZP, with the incident beam focus 9 mm downstream from the sample [Figs. 2(*a*)–2(*f*)] and centered on the sample surface [Figs. 2(*g*)–2(*h*)]. Comparison of Figs. 2(*a*) and 2(*g*) (with the sample at the specular reflection condition) and Figs. 2(*c*) and 2(*h*) (with the incident angle tilted by +0.02° and +0.025°, respectively) shows similar image contrast, indicating that the location of the condenser lens focus does not control image contrast. Similar measurements with changes in the objective lens revealed no difference in image contrast, except for a blurring of the images (not shown).

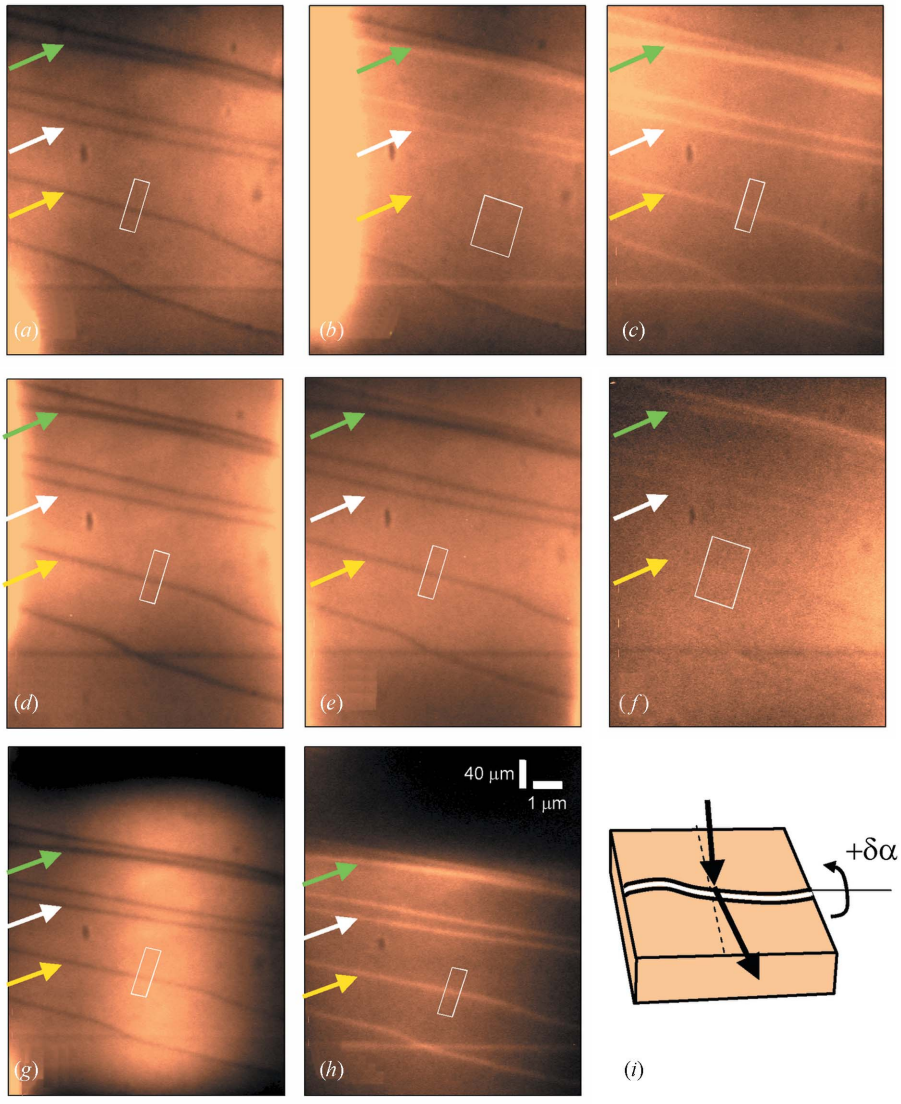

Figure 2
Images of an orthoclase (001) surface in air with the condenser lens focus 9 mm downstream from the sample position as a function of deviations of the sample angle from the specular reflection condition, $\delta\alpha$, having values of (*a*) 0.0°, (*b*) +0.01°, (*c*) +0.02°, (*d*) −0.01°, (*e*) −0.02°, (*f*) −0.03°. Also shown are two images of the same area of the surface with the condenser lens focus on the sample with $\delta\alpha$ having the values (*g*) 0.0° and (*h*) +0.025°. The direction of $\delta\alpha$ is shown schematically in (*i*) where the white line is a surface step oriented transverse to the scattering plane. Arrows indicate the three features that are discussed in the main text: the single step (yellow arrow), double step (white arrow) and multi-step (green arrow). A scale bar is shown in (*h*). Note that the differences in the variation of brightness across the images [*e.g.* (*a*)–(*f*) *versus* (*g*)–(*h*)] are associated with different illumination of the sample. In (*a*)–(*f*) the sample was illuminated with a 3 × 15 array of condenser lens positions (horizontal *versus* vertical) with associated displacements of 2 μm and 1 μm, respectively. In (*g*)–(*h*) a 1 × 30 array of condenser lens positions was used with a vertical spacing of 0.5 μm.

The images in Figs. 2(*a*)–2(*f*) are obtained at different incident angles of the X-ray beam with respect to the sample surface, indicated by the deviation of the sample angle with respect to the specular condition, $\delta\alpha = \alpha - \alpha_0$. The grey-scale contrast in each image is adjusted to maximize visibility of the various features (the variation of the reflected intensity and image contrast is shown below). The same pattern of lines appears in all of the images, but the magnitude and sign of the image contrast for these lines is controlled by $\delta\alpha$. A key observation from these images is that the change in contrast is asymmetric with respect to $\delta\alpha$. We initially focus on the contrast observed for the step indicated by the yellow arrow in Figs. 2(*a*)–2(*f*). The contrast for this step is essentially negligible at $\delta\alpha = +0.01^\circ$ (Fig. 2*b*), and changes sign to positive

contrast at $\delta\alpha = +0.02^\circ$ (Fig. 2*c*). Almost all of the features imaged as dark lines in Fig. 2(*a*) are reproduced in Fig. 2(*c*) as bright lines, indicating that only the contrast has changed. Unlike the rapid changes in contrast for $\delta\alpha > 0$, the contrast evolves more slowly for $\delta\alpha < 0$. Minimal changes in contrast are observed for sample angles as large as $\delta\alpha = -0.02^\circ$ (Fig. 2*e*), and the contrast is largely lost at $\delta\alpha = -0.03^\circ$ (Fig. 2*f*). That is, there appears to be about a threefold asymmetry in the sensitivity of image contrast to changes in the incident angle for positive *versus* negative values of $\delta\alpha$.

Line scans of the image intensity across the step of interest, shown in Fig. 3, are used to quantify these changes in contrast. These plots are normalized to the terrace intensity in each plot (and offset vertically by a constant increment of 0.15) in order to explicitly reveal the image contrast. The integration regions used for each image are shown in Fig. 2 as a white box. A larger box was used in two images where the combination of a smaller reflected intensity and reduced image contrast make it difficult to observe the steps clearly in the line scans. The step is detected as a reduction in the spatially resolved scattering intensity when observed at the specular condition (Fig. 2*a*), but the magnitude and sign of the image contrast (*e.g.* whether it is observed as a 'peak' or a 'dip') is controlled by $\delta\alpha$. Similar plots are shown for the intensity variation across two other features in these images. The change in contrast observed at the double-step (indicated by the white arrow in Fig. 2) is shown in Fig. 3(*b*) and shows a variation in contrast for each of the two steps identical to that observed for the single isolated step. The contrast variation at the multi-step (green arrow in Fig. 2) is shown in Fig. 3(*c*). Unlike the other features in Figs. 3(*a*) and 3(*b*), this structure has a contrast variation that is distinct, with both positive and negative contrast observed within a single image (*e.g.* $\delta\alpha = -0.03^\circ$). These results suggest that the image contrast is controlled by the details of the step structure and direction (*e.g.* up/down).

Images for a step that is oriented largely along the incident beam direction are shown in Figs. 4(*a*) and 4(*b*) (indicated by the yellow arrow). Line scans through this feature show that the image contrast again can be changed, transforming the destructive interference obtained at the specular condition to a constructive interference when the sample is tilted (Fig. 4*c*), with a magnitude of image contrast that is similar to that obtained with the step oriented transverse to the scattering plane. As in Figs. 2 and 3, the sample is tilted about the axis oriented along the step edge, which in this case is accomplished by a tilt in the direction transverse to the scattering plane as indicated schematically in Fig. 4(*d*). The magnitude of the sample tilt (1°) is substantially larger than that used to obtain contrast reversal for steps oriented transverse to the scattering plane (0.02°). Note also that the magnitude of the

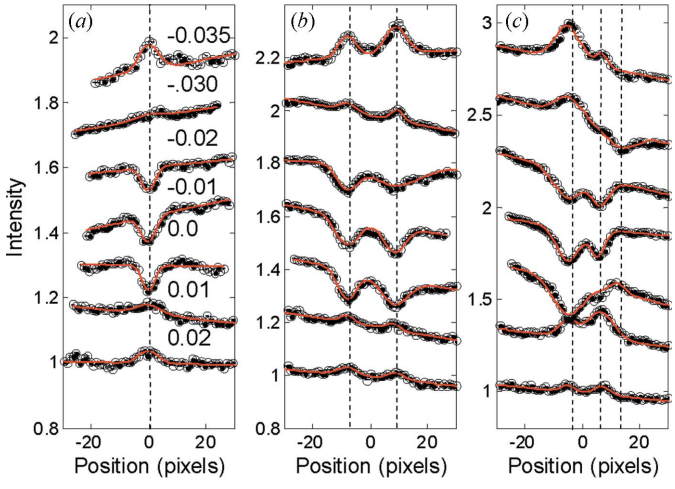

Figure 3
Intensity line scans for the (*a*) single-step, (*b*) double-step and (*c*) multi-step features indicated in the XRIM images in Fig. 2. The vertical dashed lines indicate the step locations. The same integration regions shown in Fig. 2 for the single-step structure were used to obtain line scans on all three structures in each image. The angular offset from the specular condition for each line scan is (from bottom to top): 0.02°, 0.01°, 0.0°, −0.01°, −0.02°, −0.03° and −0.035°, and are indicated in (*a*).

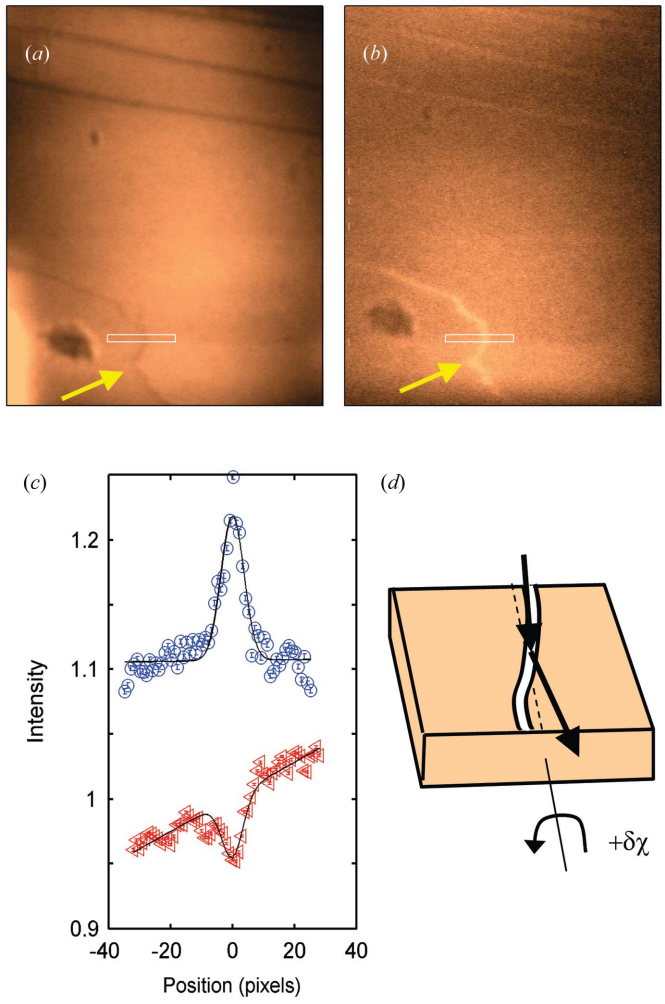

Figure 4
Images of a step aligned approximately along the scattering plane with the sample (*a*) on specular and (*b*) tilted by $\delta\chi = 1^\circ$ (in a direction transverse to the scattering plane). (*c*) Intensity line scans corresponding to the white box positions in (*a*) and (*b*), for $\delta\chi = 0$ (red triangles) and (*b*) $\delta\chi = -1$ (blue squares, offset vertically by 0.1). The condenser lens focus is on the sample position as in images in Figs. 2(*g*) and 2(*h*). (*d*) Schematic of the sample tilt direction used for the image in (*b*).

intensity enhancement in Fig. 4(*b*) is maximized when the step edge is orientated within the scattering plane [*e.g.* the region highlighted by the white box in Figs. 4(*a*) and 4(*b*)] *versus* when it is largely transverse to the scattering plane. These experimental results suggest that the image contrast is controlled by changes of the sample orientation about the axis defined by the step edge.

3.2. Model calculations of image contrast

These observations can be explained from two different perspectives. The first approach simulates the appropriate experimental details associated with the propagation of a focused wavefield incident on a surface having a topography that leads to sudden changes in the phase of the reflected wave that is propagated through the objective lens to the detector plane to obtain the image on the CCD detector (Chung & Altman, 1998; Paganin, 2006). One challenge in simulating the actual experimental conditions in this perspective includes accounting for an incoherent beam (*i.e.* having a transverse coherence length that is smaller than the beam cross section). Another challenge concerns the fact that this propagating wavefield approach is necessarily a continuum approach and implicitly requires that the phase varies over distances larger than the wavelength of the X-rays (Paganin, 2006). This condition is not satisfied when imaging a single subnanometer-high step, but the resolution of the instrument within the surface plane, $\delta x_{\|}$, is substantially larger than the wavelength and consequently the measured image is expected to be insensitive to the internal structure of the step. A more serious limitation is that this approach might not be easily extended to calculate images from specific molecular scale structures of interest (*e.g.* a nanoparticle on a surface, or a film of arbitrary structure and composition nucleating at a step).

A second approach makes use of the fact that, although the incident X-ray beam is incoherent and focused, its transverse coherence length ($\sim$100 nm) is substantially larger than the elementary steps that are being imaged ($\sim$0.65 nm). In this perspective the condenser lens illuminates a region of the sample and concentrates the incident X-ray beam so that there are sufficient photons to create an image with an appropriate magnification. The objective lens, meanwhile, images the spatial variation of the local scattering intensity $I(\mathbf{Q}_0, \mathbf{x})$ onto the CCD detector [shown schematically in Fig. 5(*a*)] as a function of the image coordinate $\mathbf{x}$ and at a momentum transfer $\mathbf{Q}_0$. The image resolution $\delta x_{\|}$ is determined by properties of the optical system. $I(\mathbf{Q}_0, \mathbf{x})$ can also be measured in a microprobe configuration where a beam with a small cross section $\delta x_{\|}$ is rastered across the surface $\mathbf{x}_{\rm sample}$ and the reflected intensity is measured with a 'point' detector with an aperture corresponding to the objective lens diameter, as shown in Fig. 5(*b*). The equivalence of these two configurations can be motivated by considering the case where the incident beam in the full-field imaging configuration [shown as blue dashed lines, Fig. 5(*a*)] has the same numerical aperture and beam cross section at the sample surface as used in the microprobe configuration (Fig. 5*b*). Here, the full-field image will consist of a single bright region on the detector $\mathbf{x}_{\rm image}$ corresponding to the beam position on the sample $\mathbf{x}_{\rm sample}$. A full image on the camera can be obtained by integrating the CCD image while scanning the incident X-ray beam position $\mathbf{x}_{\rm sample}$.

The benefit of using the microprobe configuration to simulate the experiment is that the local scattering intensity can be calculated with a straightforward extension of the kinematic scattering formalism that has been extensively developed for interpreting interfacial X-ray scattering data (Feidenhans'l, 1989; Robinson & Tweet, 1992; Als-Nielsen & McMorrow, 2001). The main drawback of this approach is that the spatial resolution of the images is derived from the numerical aperture of the FZP optics which, in the present calculations, is imposed on the calculation in the form of the effective footprint of the microprobe beam. We have chosen, nevertheless, to use this structure-factor approach to interpret

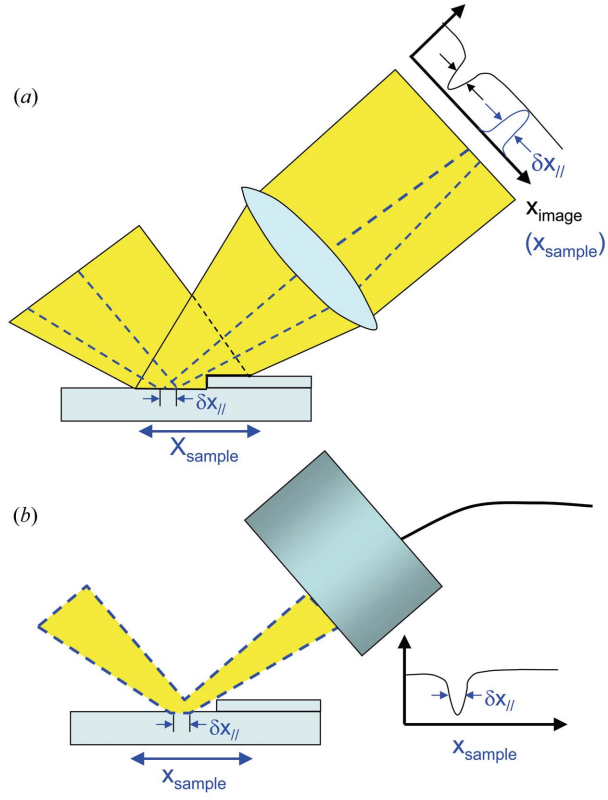

Figure 5
Schematics of (*a*) full-field and (*b*) scanning probe imaging configurations. The yellow regions indicate the X-ray beam incident to and reflecting from a surface with a single step and measured with (*a*) an area detector and (*b*) a scintillator ('point') detector. The image in (*a*) appears on the camera (as a function of detector position, $x_{\rm image}$) having a spatial resolution $\delta x_{\|}$. In the scanning probe configuration (*b*), the image is obtained by plotting the full reflected beam intensity as a function of sample position, $x_{\rm sample}$. The blue dashed lines in (*a*) indicate ray paths of an X-ray beam with the same numerical aperture and beam size as found in the microprobe configuration. In this case the reflected beam is imaged as a single bright spot on the detector (blue peak in the plot). A full image is obtained on the area detector when the sample position, $x_{\rm sample}$, is rastered, thereby 'painting' the image on the detector. [Note that the microprobe beam shown as dashed lines in (*a*) will actually fully illuminate the objective lens since the sample to objective lens distance is much larger than $\delta x_{\|}$.]

the experimental data as it provides a straightforward way to calculate the response of the microscope (*e.g.* image contrast) and provides insight into the image contrast mechanism.

Calculations of the scattering intensity within the microprobe perspective can be done within the kinematical scattering formalism through calculation of the spatially resolved interfacial structure factor, $F(\mathbf{r}_b,\mathbf{Q}) = \Sigma_j f_j A(\mathbf{r}_b,\mathbf{r}_j) \exp(i\mathbf{Q}\cdot\mathbf{r}_j) \exp[-(\mathbf{Q}\cdot\boldsymbol{\sigma}_j)^2/2]$, where the sum is over all atoms, j, illuminated by a beam described by an illumination function $A(\mathbf{r}_b, \mathbf{r}_j)$, with an average lateral beam position on the sample surface $\mathbf{r}_b$. The total structure factor can be rewritten as

$$F(\mathbf{r}_b, \mathbf{Q}) = \{F_{UC}F_{CTR} + F_{INT}\}F_{Illum}, \quad (1)$$

where the quantity in brackets is the intrinsic interfacial structure factor and $F_{Illum}(\mathbf{r}_b, \mathbf{Q}) = \Sigma_k A(\mathbf{r}_b, \mathbf{r}_k) \exp(i\mathbf{Q}\cdot\mathbf{r}_k)$ is the 'illumination structure factor' that takes into account the illumination of the surface atoms by the incident beam including the phase changes within the beam footprint associated with topography. Here, $\mathbf{r}_k$ indicates the location of surface atoms illuminated by the incident beam. For simplicity, we assume that the local interfacial structure is independent of topography (*i.e.* the local atom positions with respect to the substrate lattice are the same within terraces and at steps). As described previously (Robinson & Tweet, 1992; Fenter, 2002), the interfacial structure factor is described by a unit-cell form factor of the bulk crystal structure, F_{UC}, a term describing the structural details of the interfacial structure, F_{INT} (*e.g.* interfacial relaxations and reconstructions), and a factor that describes the semi-infinite layering of the substrate lattice, $F_{CTR} = 1/[1 - \exp(i\mathbf{Q}\cdot\mathbf{c})]$ known as the crystal-truncation rod (CTR) form factor (Robinson, 1986), where $\mathbf{c}$ is the vector displacement between successive layers. We note, for completeness, that we have observed that the CTR form factor is modified in the limit of a narrow beam cross section (*e.g.* in the context of the scanning probe illumination) in both calculations and simulations. The effect of this modification of the CTR form factor is, however, negligible for the conditions in this study, when the lateral spatial resolution $\delta x_{\|}$ is large compared with $d_{001}/\tan(\alpha)$.

We will focus on the role of interfacial topography (*i.e.* a step) in modifying the spatially resolved interfacial scattering intensity as a function of the scattering condition (*e.g.* incident angle) at a given position on the surface. In this context the observed intensities will be determined by an interplay between the relative step and X-ray beam locations, as well as the X-ray beam cross section (corresponding to the spatial resolution of the actual full-field imaging system). We make a further conceptual simplification by assuming that the beam has a cross section with sharp edges (*i.e.* all atoms within the beam are equally illuminated) so that the spatially resolved structure factor can be calculated with closed form expression. (Other beam shapes, *e.g.* Gaussian, have also been numerically simulated and do not qualitatively change the conclusions but do quantitatively change some details.)

The measured local scattering intensity is proportional to $|F|^2$ and can be written as

$$I(\mathbf{r}_b, \mathbf{Q}) \propto \int_{res} \left|\{F_{UC}F_{CTR} + F_{INT}\}F_{Illum}\right|^2 d\mathbf{Q}$$
$$\simeq I_T(Q_z) \int_{res} \left|F_{Illum}(\mathbf{r}_b, \mathbf{Q})\right|^2 d\mathbf{Q}. \quad (2)$$

Here, I_T is the intrinsic scattering intensity of an ideally flat interface (summed laterally over all atoms within the surface unit mesh and vertically for all atoms within the incident beam path), and the integration is performed over the reciprocal-space resolution volume defined by the range of incident angles associated with the focused incident beam and the solid angle of the objective lens. We will assume, for the initial model calculations, that the resolution volume is a δ-function in reciprocal space, $\delta(\mathbf{Q} - \mathbf{Q}_0)$, where $\mathbf{Q}_0$ is the nominal scattering condition. We will concentrate on the behavior of $|F_{Illum}|^2$ since the intrinsic interfacial scattering intensity is a pre-factor for a given scattering condition Q_z.

The model calculations assume a surface with a vertical layer spacing c (along $\mathbf{z}$) and a lateral lattice spacing a (along $\mathbf{x}$) with an X-ray beam having a footprint size $\delta x_{\|} = Na$ within the scattering plane, and with the step oriented so that its edge, along $\mathbf{y}$, is orthogonal to the scattering plane. When the X-ray beam is on a flat terrace region (Fig. 6*a*), the structure factor corresponds to that of an N-slit diffraction pattern (Fig. 6*c*) owing to the sum over all surface atoms illuminated by the beam. The associated illumination structure factor can be written as

$$F_{terr} = \sin(NQ_x a/2)/\sin(Q_x a/2). \quad (3)$$

[We omit pure phase factors associated with the average beam position in equations (3)–(5) since they are not observed

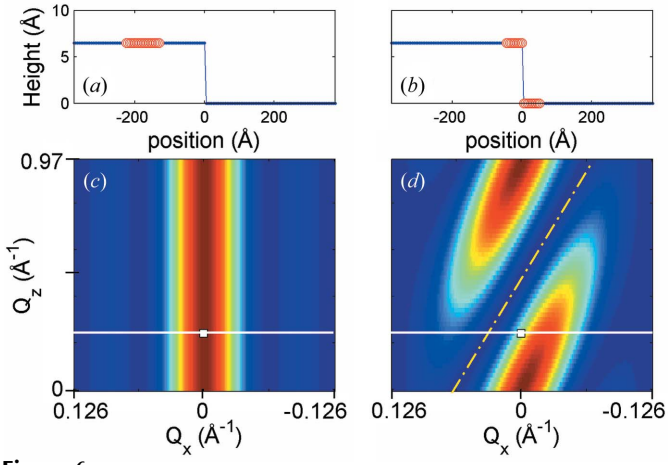

Figure 6
Model intensity calculations for a surface topography (with atom positions shown as blue points) with a single monomolecular step height of 0.65 nm at $x = 0$. The red circles indicate the illuminated region on the surface (*a*) on a terrace and (*b*) centered on a step for a beam having an assumed 10 nm lateral footprint (within the surface plane). (*c*) and (*d*) Contour plot of the calculated intensity, $I \propto |F|^2$, as a function of Q_x and Q_z (the image uses a linear color map with intensities increasing from blue to red) for the two beam positions shown in (*a*) and (*b*), respectively. The tilting and splitting of the truncation rod in (*d*) is due to the local miscut of the surface over the illuminated region. The horizontal white lines indicate the range of reciprocal space accessible by tilting the sample at $L = 0.25$. The yellow dot-dashed line in (*d*) indicates the nodal line in the step structure factor (*i.e.* zero scattered intensity).

experimentally.] This corresponds to a specular CTR oriented normal to the terrace plane with a peak intensity, $|F_{\rm terr}|^2 \simeq N^2$, and a lateral width (determined numerically) of $N\Delta Q_x a/2 = 2.8$, or $\Delta Q_x \simeq 2\pi/Na$, as expected for diffraction peak broadening owing to finite crystal size (Warren, 1990).

A second limiting case is when the beam is centered precisely at a step with a height Mc (Fig. 6*b*). In this case we obtain the illumination structure factor of

$$F_{\rm step} = 2\{\sin(NQ_x a/4)/\sin(Q_x a/2)\} \times \cos[Q_x aN/4 - MQ_z c/2]. \quad (4)$$

This is precisely the structure factor of a 'miscut' surface (Andrews & Cowley, 1985; Pflanz *et al.*, 1995; Munkholm & Brennan, 1999) in which there is one step of height Mc for every $N/2$ terrace atoms, or a miscut angle of magnitude $\tan(\alpha_{\rm miscut}) \simeq \alpha_{\rm miscut} = 2Mc/(Na)$. The first term (within the curly brackets) is maximized for $Q_x = 0$ and provides a lateral envelope within which the structure factor can be observed. The second term, however, is maximized when $Q_x aN/4 - MQ_z c/2 = 0$, or $Q_x aN/4 = MQ_z c/2$. This coupling of the vertical and lateral momentum transfer results in a tilted crystal truncation rod, as seen in Fig. 6(*d*) emanating from the origin at $\mathbf{Q} = 0$ and each Bragg peak. More generally, the interfacial structure factor changes continuously as the beam is rastered across the step since the effective miscut angle is controlled by the location of the step within the illuminated region. This can be seen through the structure factor for the beam that illuminates an area that includes a step that is n unit cells from the beam center (where $0 < |n| < N/2$),

$$F_{\rm step\_offset} = 2\{i\sin[Q_x aN/4 - MQ_z c/2][\sin(Q_x an/2)\cos(Q_x aN/4)] + \cos[Q_x aN/4 - MQ_z c/2][\cos(Q_x an/2)\sin(Q_x aN/4)]\} / \sin(Q_x a/2). \quad (5)$$

This formalism shows that the maximum tilting of the spatially resolved CTR is found when the beam is centered on the step edge ($n = 0$) corresponding to equation (4) above. These differences in the local structure factor (*i.e.* when the beam is on a terrace *versus* on the step) provide the key insight into the mechanism of image contrast for the XRIM measurements.

A key feature of this formalism is that it demonstrates that the measurement has direct sensitivity not only to the height of the step (as reported previously) but also to the step direction (*e.g.* up or down). This sensitivity derives from the one-to-one correspondence between the local physical surface normal direction (*i.e.* of the miscut surface averaged over the resolution of the instrument) with the CTR orientation. In this sense it is obvious that the measurements that include a component of the momentum transfer in a direction transverse to the step [*i.e.* Q_x in equations (3)–(5)] will have direct sensitivity to the direction of the step.

3.3. Systematic variation of step contrast

The variation of the local structure factor of a step (Fig. 7*a*) is shown as a function of Q_x for a fixed Q_z (corresponding to $L = 0.25$, indicated as the horizontal white line in Fig. 6). This shows that the structure factor of the terrace and step are generally distinct, and that the step intensity can be either higher or lower than the terrace intensity. Simulated one-dimensional real-space images are obtained by plotting the reflected intensity as a function of beam position for selected lateral momentum transfers Q_x (Fig. 7*b*), with the terrace intensity normalized to 1 in each case. These calculations reproduce many of the qualitative features found in the experimental data: the step is imaged as an approximately quadratic variation of the local intensity as a function of beam

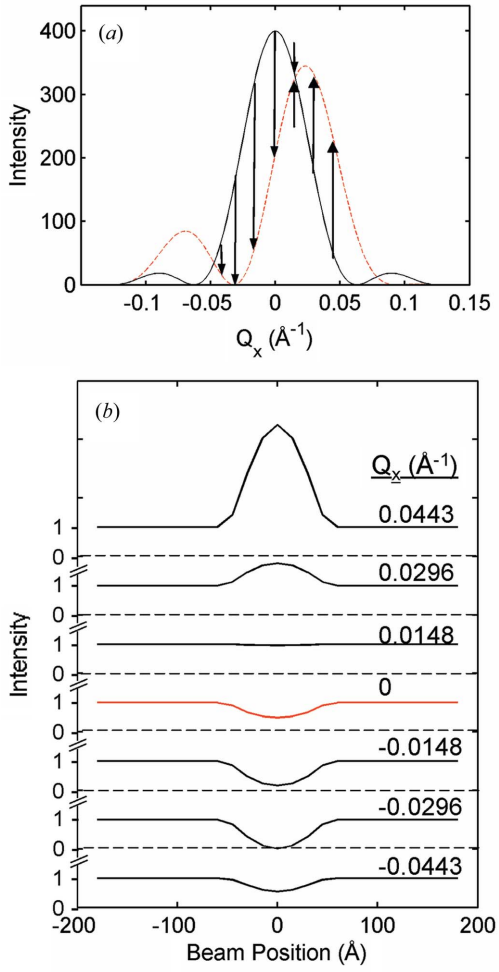

Figure 7
(*a*) Calculated intensity variation *versus* Q_x at $Q_z = 0.2412$ Å^{-1} ($L = 0.25$) for the X-ray beam on the terrace (solid black line) and on the step (dashed red line). Note that the peak of the structure factor is laterally displaced in Q_x when the beam is centered on the step (owing to the tilting of the rod as seen in Fig. 6) and that the two curves cross periodically. (*b*) Simulated one-dimensional 'images' showing the variation of the calculated intensity as the beam is scanned across a step for selected values of Q_x, indicated by the arrows in (*a*). Note how the change in step contrast, negative for $Q_x < 0.014$ Å^{-1} but positive for $Q_x > 0.014$ Å^{-1}, corresponds to whether the step structure factor is smaller or larger than the terrace structure factor at these Q_x values as shown in (*a*).

position near the step, varying monotonically between the terrace and step intensities, with a contrast that is either positive or negative, and where the maximum deviation of the intensity is found at the step location (*i.e.* beam position = 0).

The changes in step contrast are found at values of Q_x where the terrace and step structure factors have equal magnitudes. At these 'isosbestic' points, the scattering intensity of the step and terrace are identical and therefore the step can be expected to be invisible in the real-space image (*i.e.* $Q_x = 0.0148$ Å^{-1} in Fig. 7*b*). These isosbestic points define the boundaries in $\delta\alpha$ between positive and negative image contrast.

We define the contrast in an image for any scattering condition $\mathbf{Q}$ as

$$C(\mathbf{r}_b, \mathbf{Q}) \equiv \left[I(\mathbf{r}_b, \mathbf{Q}) - I_T(\mathbf{Q})\right]/I_T(\mathbf{Q}), \tag{6}$$

where $I(\mathbf{r}_b, \mathbf{Q})$ is the observed intensity at the defect location, $\mathbf{r}_b$. With this definition, $C < 0$ when the step is darker than the terrace and $C > 0$ when the step is brighter than the terrace. The maximum negative contrast is found when $I(\mathbf{r}_b, \mathbf{Q}) = 0$, where $C = -1$. When including the structure factors for an X-ray beam on a flat terrace and centered on a single M unit-cell high step [equations (3) and (4)], we obtain

$$C_{step} = \left\{\cos^2\left[Q_x aN/4 - MQ_z c/2\right] - \cos^2(NQ_x a/4)\right\} / \cos^2(NQ_x a/4). \tag{7}$$

From this function the isosbestic points are found when $C_{step} = 0$, or equivalently when $Q_x aN/4 - MQ_z c/2 = \pm NQ_x a/4 \pm \pi$. Two solutions satisfying this condition that are closest to the specular condition are [using $Q_x = \sin(\delta\alpha)Q_z \simeq \delta\alpha Q_z$, and $\delta x_\parallel = Na$]

$$\delta\alpha_{iso-1} \simeq Mc/\delta x_\parallel, \tag{8a}$$

$$\delta\alpha_{iso-2} \simeq [(ML - 1)/L]c/\delta x_\parallel. \tag{8b}$$

For $L = 0.25$, this formalism predicts that isosbestic points will be found at $\delta\alpha_{iso} = c/\delta x_\parallel$ and $-3c/\delta x_\parallel$. This confirms the trends observed both in the experimental data (Figs. 2, 3 and 4) and the calculations (Figs. 6 and 7) that changes in the image contrast are asymmetric with respect to the sample angle $\delta\alpha$. The polarity of the step is determined by the displacement of the observed specular rod (*i.e.* a downward step, from the perspective of the incident beam, locally tilts the reflected X-ray beam towards the surface plane).

The variation of interfacial contrast as a function of vertical momentum transfer, Q_z (with the sample held at the specular reflection condition for terraces), was previously used to identify the step height in an image (Fenter *et al.*, 2006). The theoretical maximum negative contrast, $C = -1$, can be obtained for a monomolecular step only at the 'anti-Bragg' condition, $Q_z = \pi/c$ (or $L = 0.5$) when $Q_x = 0$. More generally, equation (7) reveals that full negative contrast can also be obtained at any Q_z by choosing Q_x such that $\cos[Q_x aN/4 - Q_z c/2] = 0$ (*i.e.* $Q_x = -0.0296$ Å^{-1} in Fig. 7*b*). Physically, this condition occurs when the parts of the X-ray beam on opposite sides of a step are exactly out of phase. This leads to a nodal line separating the two miscut rods (dot-dashed yellow line, Fig. 6*d*). This also shows that contrast variation as a function of Q_x is symmetric at $L = 0.5$. It is convenient to calculate the angular change of the incident angle necessary to achieve maximum negative contrast ($C = -1$). The two nodes of the step structure factor closest to the specular condition are defined by

$$\delta\alpha_{node} \simeq c[(2ML \pm 1)/L]/\delta x_\parallel. \tag{9}$$

At $L = 0.25$, this results in a node at a sample angle of $\delta\alpha_{node} \simeq -2c/\delta x_\parallel$. Similar expressions will be found for the case of maximum positive contrast (*i.e.* $C = \infty$, when the terrace intensity is zero).

These results reveal that XRIM images at fixed vertical momentum transfer, Q_z, can be converted, in principle, to maps of the surface topography. This can be accomplished by obtaining XRIM images as a function of the sample angle (including $\delta\alpha$ and $\delta\chi$), and observing the angular displacements corresponding to the isosbestic points for each step. Using the simple relationship in equation (8), the height and polarity (*e.g.* up *versus* down) of each step can be determined directly. This approach may, in practice, be complicated by topographies in which the step orientations are not well aligned along either within or transverse to the scattering plane. These results demonstrate the principle that the recovery of topographic profiles does not necessarily require that XRIM images be obtained at multiple vertical momentum transfers Q_z as was reported previously (Fenter *et al.*, 2006).

We have so far described image contrast as a simple peak or dip in the local intensity *versus* position. It is, however, possible to obtain more complex real-space images that have an intensity variation that oscillates as a function of position away from the step, with both negative and positive contrast in a given image. This has been seen previously in calculations of LEEM images obtained with a wave-optical model (Chung & Altman, 1998). Within the context of the present calculations, these oscillations occur when the lateral phase variation across the resolution element, $\delta x_\parallel$, is large (*i.e.* $Q_x \delta x_\parallel > \pi$). In this context the isosbestic points described by equation (8) correspond strictly to the case where the beam is centered on the step. This leads to non-zero image contrast at these nominal isosbestic points (*e.g.* a single step imaged as two dark lines on either side of the step). We note that this more complex behavior is largely avoided when including the actual experimental details included as the limits of integration in equation (2). This will be discussed below.

3.4. Comparison between data and model calculations

The results in the previous section explicitly reveal that the magnitude and sign of intensity contrast depends on the interrelationships between the scattering condition $\mathbf{Q}$ of the object being observed (*e.g.* the step height and direction), as well as the spatial resolution of the microscope projected on the surface plane, $\delta x_\parallel$. This can be understood since the width of the specular CTR also depends inversely on this parameter [as seen in equation (3)], and consequently, the ability to change

interfacial contrast depends on moving the detector resolution function off the specular rod of the flat terrace regions.

With these observations in mind, we can further assess the structure factor model for explaining the image contrast by directly comparing the observed and calculated contrast. Intensity line scans in Fig. 3(*a*) are shown for different sample angles $\delta\alpha$ corresponding to the single isolated step in Fig. 2. The experimentally determined contrast and terrace intensity are quantified through fits of these data using a Gaussian function (with peak height $I_P = I_{step} - I_T$) associated with the step and a linearly varying background associated with the terrace intensity I_T and an experimentally observed step contrast $C = I_P/I_T$. (The slope in the line scan is associated with variations of the incident beam illumination and is not an intrinsic characteristic of the interfacial structure or step contrast.) The results of these fits are shown in Fig. 8 as a function of the angular deviation from the specular condition $\delta\alpha$. Each data point was obtained on distinct regions of the image with no overlap of the integrated regions, using the same integration region size indicated on each image in Fig. 2. Data were also obtained for two different positions of the condenser FZP, with the incident beam focus 9 mm downstream from the sample [for the images in Figs. 2(*a*)–2(*f*)] and with the beam focus centered on the sample surface [Figs. 2(*g*)–2(*h*)]. Since the images are not normalized for variation of illumination across the image, there is a significant variation of measured terrace intensity for different areas on the image (Fig. 8*a*). Nevertheless, the data clearly show that the terrace intensity as a function of sample angle $\delta\alpha$ has an approximately Gaussian shape centered on the specular condition having a full width at half-maximum of $\sim 0.04^\circ$. This spatially resolved rocking scan is similar to that used to distinguish between the specular intensity and the background diffuse scattering, whose width is controlled by the detector slit size. From the objective lens size and distance to the sample, we expect an angular rocking width of $\sim 0.06^\circ$. The smaller nominal width found in the experimental data is likely due, in part, to the neglect of any background signal in the line fit to the data in Fig. 8(*a*).

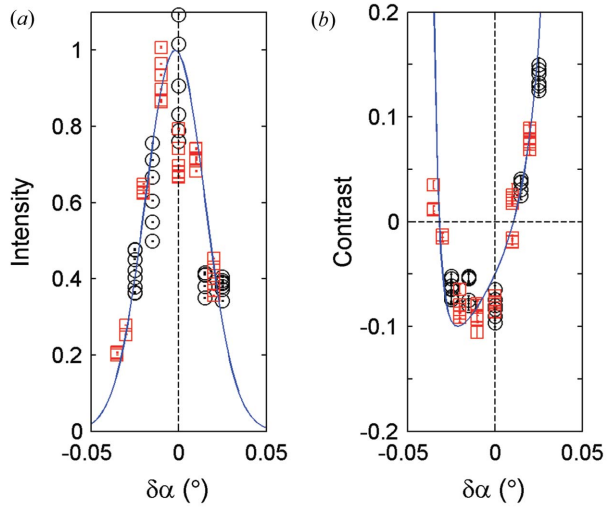

Figure 8
Measured (*a*) reflected terrace intensity and (*b*) step contrast as a function of sample angle, $\delta\alpha$, for the condenser focus position on the sample (black circles) and 9 mm downstream (red squares). The data points are derived from the least-squares fitting of the intensity line scans (*e.g.* Fig. 3) using one or two Gaussian peaks and a linear background. The solid line in (*a*) is a Gaussian function with a full width at half-maximum of 0.04°. Multiple data points at each sample angle correspond to independent points on the same image and the differences are due to non-uniform illumination. Note how the contrast variation is asymmetric with respect to the incident angle. The blue line is derived from the model calculations with an X-ray optical resolution of 100 nm (or ~4200 nm projected onto the surface plane) and an assumed maximum contrast of 0.1.

The contrast as a function of sample angle is shown in Fig. 8(*b*) for the same data points in Fig. 8(*a*). Since the contrast is the ratio of step to terrace intensities, variations in reflected signal owing to incident beam illumination are removed. Instead we find a well defined asymmetric variation of the sample angle $\delta\alpha$ that is distinct from the symmetric variation of terrace intensity (Fig. 8*a*). Specifically, the contrast changes rapidly for $\delta\alpha > 0$ with a change of sign at $\delta\alpha \simeq 0.01^\circ$. Meanwhile the contrast is initially flat for $\delta\alpha < 0$, but eventually decreases in magnitude and changes in sign near $\delta\alpha \simeq -0.03^\circ$. Quantitatively similar variations in contrast are obtained for the two condenser lens positions, demonstrating that the image contrast is independent of the defocus of the incident condenser lens.

We can use these data to estimate the appropriate experimental parameters for the XRIM images. From equation (8), we expect zero image contrast for $\delta\alpha = c/\delta x_{\|}$ and $-3c/\delta x_{\|}$ for our scattering condition (L = 0.25 r.l.u.). With the observed contrast node locations at approximately 0.01° and −0.03, we obtain $\delta x_{\|}$ = 3600 nm (using c = 0.6495 nm). Projected on the detector plane, this leads to a spatial resolution of $\delta x_{FZP} = \delta x_{\|}\sin(\alpha)$ = 86 nm which is similar to the expected resolution for our experimental condition (~100 nm). While this explains the asymmetry associated with incident angles where the image contrast is zero, it strongly over-estimates the magnitude of the contrast, especially the predicted value of $C = -1$ at $\delta\alpha = -2c/\delta x_{\|} = -0.02^\circ$. Although the sample angle of maximum negative contrast is consistent with experimental data, the observed contrast is substantially smaller in magnitude than expected from these simple model calculations, as was found previously (Fenter *et al.*, 2006). If we scale the absolute contrast by a numerical factor, C_{max} = 0.1, the variation in contrast as a function of sample angle is largely explained, as indicated by the solid blue line in Fig. 8(*b*). The need to invoke an arbitrary scale factor is, however, unsatisfactory.

3.5. Realistic calculations of image contrast

We have so far ignored the integration over the finite reciprocal-space resolution function in equation (2). The appropriateness of this assumption can be evaluated based on the actual experimental parameters using the reciprocal-space construction in Figs. 9(*a*) and 9(*b*). The range of reciprocal-space resolution function is determined by the finite incident-beam divergence, $\Delta\alpha \simeq 1/805$, and the angular acceptance of

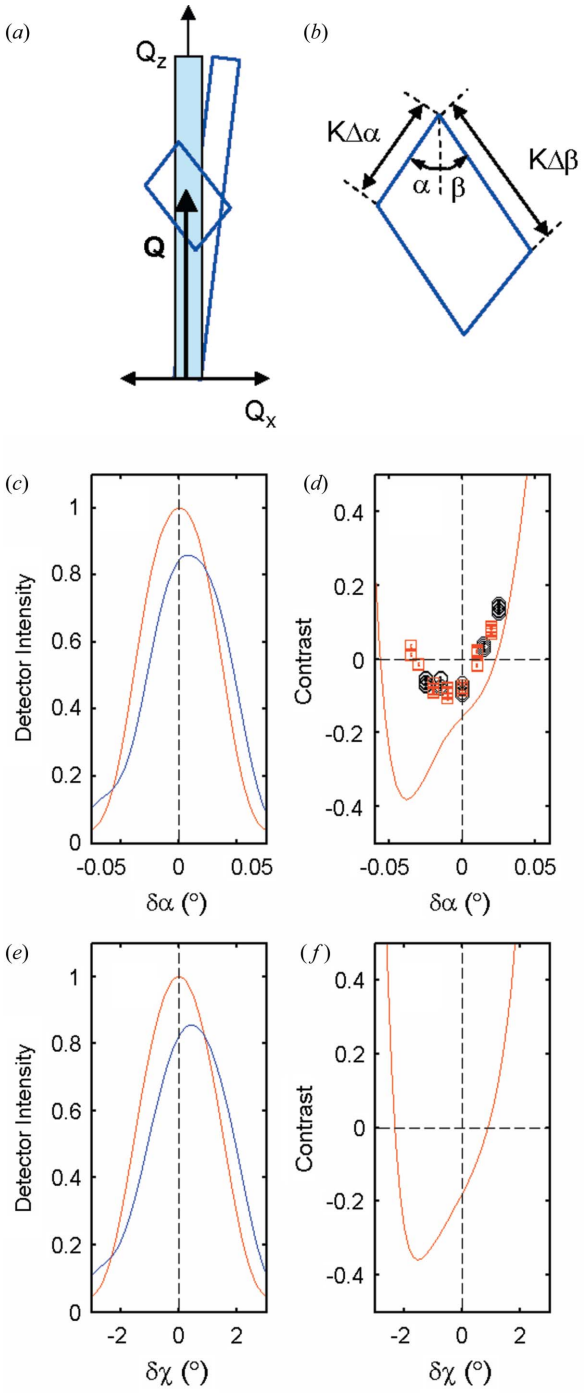

Figure 9
(*a*) Illustration of the reciprocal-space resolution associated with the realistic experimental conditions of the XRIM experiment, including the incident and reflected beam divergence ($\Delta\alpha$ and $\Delta\beta$, respectively) and the finite width of the specular rod associated with the real-space resolution of the X-ray optics. (*c*) Simulations of the rocking scan shape for the beam on the flat terrace and centered on a step (red and blue lines, respectively) and (*d*) image contrast expected as a function of the in-plane sample angle, $\delta\alpha$, for a step oriented orthogonal to the scattering plane (Fig. 2*i*) using the actual experimental parameters used in the present experiments. The data are the same as that found in Fig. 8(*b*). Simulations of (*e*) rocking scan and (*f*) image contrast as a function of the out-of-plane sample angle, $\delta\chi$, for a step oriented in the scattering plane (Fig. 4*d*). Note the similarity of the XRIM response for these cases, except for the range of the sample tilt needed to obtain contrast reversal ($\pm 0.05^\circ$ and $\pm 2^\circ$, for $\delta\alpha$ and $\delta\chi$, respectively).

the detector, $\Delta\beta \simeq 0.08/34 \simeq 1.9\,\Delta\alpha$. The vertical width of the resolution function can be written as $\Delta Q_z \simeq K(\Delta\alpha + \Delta\beta)\cos[(\alpha + \beta)/2] = 0.018$ Å^{-1}, corresponding to $\sim Q_{001}/50$ (where $Q_{001} = 2\pi/d_{001}$). This can be safely ignored since the vertical extent of the crystal truncation rod from surface and/or step varies slowly and continuously with Q_z, as seen in Fig. 6. The lateral width of the resolution function varies as $\Delta Q_x = K(\Delta\alpha + \Delta\beta)\sin[(\alpha + \beta)/2] = 0.000448$ Å^{-1}. This is much smaller than ΔQ_z, but it corresponds to an effective angular broadening of 0.1° for the conditions of the experiment ($L = 0.25$ r.l.u.). Since a significant variation in contrast was observed for changes in the incident angle of about tenfold smaller than this (Fig. 8*b*), the shape and extent of the reciprocal-space resolution function cannot be ignored for these experimental conditions. We can anticipate that inclusion of this factor will tend to blur the observed reciprocal-space structure, reducing the step contrast for our experimental conditions.

We first define a quantity $\Xi \equiv \delta Q_{\|\_\mathrm{tilt}}/\Delta Q_{\|\_\mathrm{res}}$ to evaluate the significance of the reciprocal-space resolution, where $\delta Q_{\|\_\mathrm{tilt}}$ is the lateral displacement of the specular rod when the beam is on a step *versus* on a terrace, and $\Delta Q_{\|\_\mathrm{res}}$ is the lateral width of the resolution function. From this definition the image will exhibit ideal contrast (*e.g.* $C = -1$) if $\Xi > 1$, while the fractional contrast will be reduced by a factor of Ξ if $\Xi < 1$ (*i.e.* the displacement of the rod is smaller than the lateral width of the resolution function). From the discussion above, $\delta Q_{\|\_\mathrm{tilt}} = Q_z(2c/\delta x_\|) = 4\pi L/\delta x_\|$ for $Q_z \leq \pi/c$ (or equivalently, $L \leq 1/2$), where $Q_z = (2\pi/c)L$ and $\delta x_\| = \delta x_{\mathrm{FZP}}/\sin(\alpha)$ is the projection of the experimental optical resolution to the surface plane and $\delta x_{\mathrm{FZP}} = \lambda/\Delta\alpha$ is the outer zone width of the FZP that corresponds in this context to the incident beam coherence length (*i.e.* owing to the incident beam focus). The lateral extent of the resolution function is $\Delta Q_{\|\_\mathrm{res}} \simeq 2\pi\sin(\theta)(1/\delta x_{\mathrm{FZP1}} + 1/\delta x_{\mathrm{FZP2}}) \simeq 2\pi(1/\delta x_{\|1} + 1/\delta x_{\|2})$. For the ideal case where the numerical aperture of the two lenses are matched, $\delta x_{\|1} = \delta x_{\|2}$, we find $\Delta Q_{\|\_\mathrm{res}} \simeq 4\pi/\delta x_\|$, or $\Xi \simeq L$ (*i.e.* the contrast varies as $C \simeq \Xi C_0$, where C_0 is the contrast obtained in the model calculations above that ignored Q-resolution). That is, the use of realistic condenser and objective lenses leads to a maximum observable contrast for a step (oriented transverse to the scattering plane) of $C \simeq -0.5$ at $L = 0.5$, as compared with $C_0 = -1$ obtained when the beam divergence and reciprocal-space resolution are ignored. That is, the use of focusing optics intrinsically reduces the image contrast with respect to that calculated above. The ability to attain $C = -1$ is limited to the unrealistic situation in which an incident beam, that is both highly collimated and having a small lateral width, is rastered across the surface step, corresponding to the results in Figs. 6 and 7. In the present measurements the numerical aperture of the objective zone plate was twice that of the condenser lens. This does not influence the effective CTR rod width (since the objective lens is not fully illuminated), but it does increase the lateral width of the resolution function, $\Delta Q_\| \simeq 2\pi\sin(\theta)(1/\delta x_{\|1} + 1/\delta x_{\|2}) \simeq 6\pi/\delta x_\|$, leading to an expected maximum contrast of $-2L/3$. For the present measurements at $L = 0.25$, we therefore expect

a contrast of ~ -0.17 on the specular condition ($\delta\alpha = 0$) for our detailed experimental conditions. This compares favorably in absolute units with the observed contrast of ~ -0.08.

We have also used closed-form calculations using equations (2) and (5) to simulate the influence that the actual experiment optical parameters have on these images (Fig. 9). Here, the rocking scan is calculated for the beam on the terrace and at the step as a function of Q_x for the experimental parameters used in the measurements of Figs. 2 and 4. This calculation includes the full three-dimensional details of the structure factor and the experimental resolution function (the latter of which includes the incident beam focusing, the circular cross section of the condenser and objective lenses, the central beam stop in the condenser lens, and the finite range of detector angles accepted by the objective lens). The only adjustable parameter in the calculation is the spatial resolution of the imaging system. We use a spatial resolution of $\delta x_{\rm FZP} = 100$ nm corresponding to the condenser FZP since the numerical aperture of the objective FZP is approximately double that of the condenser FZP. The observed image resolution, consequently, is limited by the numerical aperture of the incident beam owing to incomplete filling of the objective lens.

These results show that the rocking scan becomes broadened owing to the finite extent of the resolution function [Figs. 9(*c*) and 9(*e*)]. The general trends described above are confirmed, especially the control of image contrast through changes in Q_x (or equivalently $\delta\alpha$). A direct result of this broadening of the rocking scan is that the relative contrast is reduced with respect to the ideal behavior found in Figs. 6 and 7. In particular, the contrast on the specular condition at $L = 0.25$ is found to be $C = -0.14$. This is much smaller than the theoretical value of -0.5 obtained from the model structure-factor calculations (ignoring experimental parameters). This simulation result is similar to the simple estimate (above) of -0.17, and is reasonably close to the experimentally observed value of -0.08. That is, inclusion of the relevant experimental details explains most of the differences between the experimentally observed contrast and the ideal theoretical image contrast, at least for the specular imaging condition.

While the calculated contrast variation as a function of Q_x (or $\delta\alpha$) is similar to that observed experimentally (Fig. 9*d*), there remain some notable discrepancies. The calculation continues to reveal a variation of the contrast as a function of incident angle that is both more asymmetric, with isosbestic points that occur at larger angular displacements, and with contrast magnitudes that are larger than that observed experimentally. The maximum calculated contrast, -0.4, can be compared with the maximum experimental contrast of -0.1. The simulated isosbestic points for zero contrast found at $\delta\alpha \simeq 0.025^\circ$ and -0.05° are approximately twofold larger than the observed values ($\delta\alpha \simeq +0.01^\circ$ and -0.03°). It is expected that these discrepancies are associated with differences between the actual reciprocal-space resolution function of the experiment and that used in the calculation. In particular, these differences between observed and calculated image contrast variations suggest that the spatial resolution in the observed images is poorer than expected. We expect that these discrepancies may also be associated with misalignment of the step orientation with respect to the scattering plane (*i.e.* the calculations assume that the step edge is strictly orthogonal to the scattering plane), especially since the image magnification is very asymmetric.

We also calculate the contrast variation for a step that is oriented within the scattering plane [Figs. 9(*e*) and 9(*f*)], corresponding to the data in Fig. 4, and observed previously (Fenter *et al.*, 2006). In this case, because the tilting of the step structure factor is transverse to the scattering plane, the variation of contrast will occur as the sample is tilted by an out-of-plane angle $\delta\chi$ (achieved in this case by using the four-circle spectrometer motor χ). While many aspects of the contrast variation are similar for the two cases, the angular range over which contrast changes are observed is larger (*i.e.* $\delta\alpha \simeq \pm 0.05^\circ$ while $\delta\chi \simeq \pm 2^\circ$). This is due simply to the relative sensitivity of moving the specular rod off the resolution function for these two spectrometer directions, as reproduced in Fig. 9(*f*), and illustrates directly that the contrast is observed when the rod is displaced outside of the resolution function defined by the numerical apertures of the condenser and objective lenses. An additional test of this formalism is to calculate the maximum expected contrast for a step aligned along the scattering plane in the specular reflection condition ($\delta\chi = 0$), in comparison with that measured previously, where a maximum contrast of $C \simeq -0.3$ was observed in the specular geometry at $L = 0.5$ (Fenter *et al.*, 2006). The present calculations show a calculated contrast of -0.3 which is in excellent agreement with those previous observations.

3.6. Non-zero image contrast for pure phase objects

It is well known in coherent X-ray microscopy that pure phase objects (*i.e.* those that do not absorb X-rays) have no contrast when the detector is placed on the image plane (Paganin, 2006). This result can be understood when considering that the role of the X-ray optics is to reproduce and magnify the spatial variations of the X-ray field intensity from the object plane to the image plane. In the limit of no absorption for an ideally thin sample, the wavefield just outside of the sample will be modified only in terms of its phase but not intensity. The conditions assumed in this derivation clearly apply to the present measurements, as the reflected X-ray beam will exhibit negligible attenuation by the sample and the changes in the observed images have been attributed solely to phase contrast associated with elementary topography. This apparent paradox raises the question of why any experimental contrast is achieved in these measurements. More generally it is known that any aberrations in an optical system (*i.e.* as defined by the transfer function for the propagation of coherent X-ray fields) can lead to intensity contrast in measured images. It is therefore useful to identify the nature of the optical aberrations that lead to the observed image contrast in the present measurements.

The structure-factor formalism that we have used provides a natural resolution to this apparent paradox. Implicit in the derivation of this result for pure phase objects is the

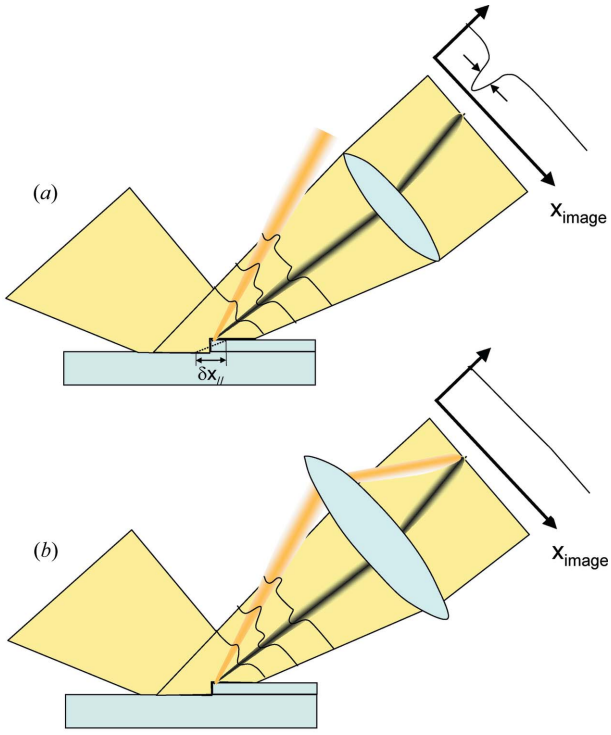

Figure 10
Schematic illustration revealing the relationship between image contrast and objective lens acceptance illustrated within the context of geometrical optics for each resolution element, $\delta x_{||}$. (*a*) When the in-plane spatial resolution is sufficiently small, the observed image contrast derives from the deflection of the X-ray beam reflected in the vicinity of the step to an angle outside of the objective lens aperture. Here the orange and black regions of the reflected X-ray field indicate the increase and decrease of reflected photon intensity, respectively, with respect to that associated with scattering from a flat terrace region. The enhanced X-ray field is reflected at a different angle owing to the locally tilted surface plane (indicated by the dashed line) within a single resolution element that includes the step. The step is observed as a dark line on the image since the X-rays reflected from the step are deflected outside of the objective lens aperture. If the objective lens were made sufficiently large so as to accept the locally reflected beam, the image contrast would be eliminated since all photons reflected from this region would be imaged at the step location on the image plane.

assumption that the objective lens is sufficiently large to fully accept the entire reflected beam. That this condition was not satisfied can be seen in the idealized structure-factor calculations (Fig. 6) where a tilting of the specular rod is associated with an angular displacement of the reflected beam reflected from the vicinity of the step. The implicit assumption in these calculations of a finite detector acceptance corresponding to a δ-function (*i.e.* one pixel in the images of Fig. 6) leads to full contrast (*i.e.* $C = -1$) at any Q_z as long as the detector is placed along the nodal line in the interfacial structure factor (yellow line in Fig. 6). Physically, this means that the reflected beam in the vicinity of the step is displaced outside of the objective lens acceptance and therefore is excluded from the image (leading to dark steps). Inclusion of the actual size of the reciprocal-space resolution function associated with the focused beam and detector acceptance used in the experiment reduces, but does not eliminate, image contrast because the actual objective lens is sufficiently small that a portion of the reflected beam continues to be displaced outside of the detector acceptance in the vicinity of the step (Fig. 9*a*).

This reveals that the experimentally observed contrast is obtained owing to the incomplete collection of the beam reflected from the vicinity of the step (*i.e.* the objective lens acts as a slit) leading to limited aperture contrast microscopy. In order to test whether this alone is sufficient to resolve this nominal paradox, we simulated the effect of having a fivefold larger vertical detector acceptance than was used in the experiment (with no changes in assumed real-space resolution). With only this change in the simulated experiment, the calculated images show no observable contrast, reproducing the expectation based on coherent X-ray optics for imaging pure phase objects. That is, the observed contrast is derived solely from the displacement of a portion of the beam outside of the objective lens.

This concept is illustrated schematically in Fig. 10. When the deflection of the beam reflected from the vicinity of an isolated step (with an angular deflection corresponding to the ratio of the step height to the lateral spatial resolution) is large enough that it exceeds the objective lens aperture, then the imaging system reveals a dark region in the vicinity of the step (Fig. 10*a*). The step becomes invisible, however, if the objective lens were made sufficiently large as to accept the locally reflected beam (Fig. 10*b*). A similar result is obtained if the coherence of the incident beam is increased sufficiently that the local beam deflection remains within the objective lens. In the limit of a fully coherent beam, the reflected beam is deflected as a whole so that the net angular deviation is negligible, leading to an absence of image contrast.

4. Summary and conclusions

Experimental data and calculations have been presented providing new insight into the control of image contrast when imaging molecular-scale features using X-ray reflection interface microscopy. Experimental data of elementary steps on an orthoclase (001) surface show that the image contrast (in both sign and magnitude) is systematically controlled by the lateral momentum transfer (*i.e.* changes in both the sample orientation with respect to the incident X-ray beam) and the details of the step structure including alignment (within, or transverse to, the scattering plane), direction (*e.g.* up or down) and height. A formalism for calculating the image contrast of molecular-scale features, based on a simple extension of the kinematic scattering formalism, was presented to quantify interfacial X-ray scattering data, and was used to predict the image contrast for monomolecular steps. Model calculations in this formalism provide insight into the mechanism of image contrast and reveal the sensitivity of the image contrast to the step direction (*e.g.* up or down). The inclusion of the actual reciprocal-space resolution volume (owing to the focus of the incident beam by the condenser lens and the angular acceptance of the objective lens) provides a reasonable explanation (in absolute units) of the observed changes in local image contrast, demonstrating that this is a primary factor control-

ling the magnitude of image contrast. These results show that the image contrast is independent of the focal position of the condenser lens with respect to the sample surface. The ability to reproduce the magnitude and angular variation of interfacial contrast suggests that the mechanism of image contrast reveals that the instrument is operating near its expected characteristics given the known experimental parameters (*e.g.* optical characteristics). This suggests that the full surface topography can be recovered from a series of images with appropriate sample orientations at fixed momentum transfer magnitude (with the number of images needed depending on the range of step heights found in the images). This formalism also shows that the ability to image surface topography (which is a pure phase object) derives from the finite acceptance of the objective lens that acts as a slit. This formalism can be extended to predict and understand the image contrast for molecular-scale objects with arbitrary structure and shape.

This work was supported by the Geosciences Research Program of the Office of Basic Energy Sciences, US Department of Energy (DOE), through contract DE-AC02-06CH11357. The data were collected at the X-ray Operations and Research (XOR) beamlines 12-ID-D (BESSRC/XOR) at the Advanced Photon Source (APS), Argonne National Laboratory. Use of the Advanced Photon Source is also supported by the US Department of Energy, Office of Science, Office of Basic Energy Sciences, under Contract DE-AC02-06CH11357. We thank Steve Wang, Michael Feser and Wenbing Yun (Xradia) for their assistance in developing and subsequent optimization of this instrument, as well as Yong Chu and Franz Pfeiffer for useful discussions.

References

Als-Nielsen, J. (1987). *Top. Curr. Phys.* **43**, 181–222.
Als-Nielsen, J. & McMorrow, D. (2001). *Elements of Modern X-ray Physics.* New York: John Wiley and Sons.
Andrews, S. R. & Cowley, R. A. (1985). *J. Phys. C*, **18**, 6427–6439.
Attwood, D. T. (1999). *Soft X-rays and Extreme Ultraviolet Radiation: Principles and Applications.* Cambridge University Press.
Bauer, E. (1994). *Rep. Prog. Phys.* **57**, 895–938.
Braslau, A., Pershan, P. S., Swislow, G., Ocko, B. M. & Als-Nielsen, J. (1988). *Phys. Rev. A*, **38**, 2457–2470.
Chen, X. D. & Gibson, J. M. (1998). *Phys. Rev. Lett.* **81**, 4919–4922.
Chiaramonti, A. N. & Marks, L. D. (2005). *J. Mater. Res.* **20**, 1619–1627.
Chu, Y. S., You, H., Tanzer, J. A., Lister, T. E. & Nagy, Z. (1999). *Phys. Rev. Lett.* **83**, 552–555.
Chung, W. F. & Altman, M. S. (1998). *Ultramicroscopy*, **74**, 237–246.
Do, D. H., Evans, P. G., Isaacs, E. D., Kim, D. M., Eom, C. B. & Dufresne, E. M. (2004). *Nat. Mater.* **3**, 365–369.
Eisebitt, S., Luning, J., Schlotter, W. F., Lorgen, M., Hellwig, O., Eberhardt, W. & Stohr, J. (2004). *Nature (London)*, **432**, 885–888.
Eres, G., Tischler, J. Z., Yoon, M., Larson, B. C., Rouleau, C. M., Lowndes, D. H. & Zschack, P. (2002). *Appl. Phys. Lett.* **80**, 3379–3381.
Feidenhans'l, R. (1989). *Surf. Sci. Rep.* **10**, 105–188.
Fenter, P. A. (2002). *Rev. Mineral. Geochem.* **49**, 149–220.
Fenter, P., Park, C., Zhang, Z. & Wang, S. (2006). *Nat. Phys.* **2**, 700–704.
Fenter, P., Teng, H., Geissbuhler, P., Hanchar, J. M., Nagy, K. L. & Sturchio, N. C. (2000). *Geochim. Cosmochim. Acta*, **64**, 3663–3673.
Fienup, J. R. (1978). *Opt. Lett.* **3**, 27.
Gerchberg, R. W. & Saxton, W. O. (1972). *Optik*, **35**, 237–246.
Jacobsen, C., Williams, S., Anderson, E., Browne, M. T., Buckley, C. J., Kern, D., Kirz, J., Rivers, M. & Zhang, X. (1991). *Opt. Commun.* **86**, 351–364.
Kang, H. C., Maser, J., Stephenson, G. B., Liu, C., Conley, R., Macrander, A. T. & Vogt, S. (2006). *Phys. Rev. Lett.* **96**, 127401.
Kirz, J., Ade, H., Jacobsen, C., Ko, C. H., Lindaas, S., McNulty, I., Sayre, D., Williams, S., Zhang, X. & Howells, M. (1992). *Rev. Sci. Instrum.* **63**, 557–563.
Lyman, P. F., Shneerson, V. L., Fung, R., Harder, R. J., Lu, E. D., Parihar, S. S. & Saldin, D. K. (2005). *Phys. Rev. B*, **71**, 081402(R).
McNulty, I., Kirz, J., Jacobsen, C., Anderson, E. H., Howells, M. R. & Kern, D. P. (1992). *Science*, **256**, 1009–1012.
Manceau, A., Marcus, M. A. & Tamura, N. (2002). *Rev. Mineral. Geochem.* **49**, 341–428.
Miao, J. W., Charalambous, P., Kirz, J. & Sayre, D. (1999). *Nature (London)*, **400**, 342–344.
Munkholm, A. & Brennan, S. (1999). *J. Appl. Cryst.* **32**, 143–153.
Ocko, B. M., Wang, J., Davenport, A. & Isaacs, H. (1990). *Phys. Rev. Lett.* **65**, 1466–1469.
Paganin, D. (2006). *Coherent X-ray Optics.* Oxford University Press.
Park, C., Fenter, P. A., Nagy, K. L. & Sturchio, N. C. (2006). *Phys. Rev. Lett.* **97**, 016101.
Pflanz, S., Meyerheim, H. L., Moritz, W., Robinson, I. K., Hoernis, H. & Conrad, E. H. (1995). *Phys. Rev. B*, **52**, 2914–2926.
Robinson, I. K. (1986). *Phys. Rev. B*, **33**, 3830–3836.
Robinson, I. K. (1991). *Handbook on Synchrotron Radiation*, Vol. 3, *Surface Crystallography*, edited by G. S. Brown and D. E. Moncton, pp. 223–266. Amsterdam: North Holland.
Robinson, I. K. & Tweet, D. J. (1992). *Rep. Prog. Phys.* **55**, 599–651.
Robinson, I. K., Vartanyants, I. A., Williams, G. J., Pfeifer, M. A. & Pitney, J. A. (2001). *Phys. Rev. Lett.* **87**, 195505.
Ross, F. M. & Gibson, J. M. (1992). *Phys. Rev. Lett.* **68**, 1782–1785.
Rotermund, H. H., Engel, W., Jakubith, S., Vonoertzen, A. & Ertl, G. (1991). *Ultramicroscopy*, **36**, 164–172.
Sayre, D., Chapman, H. N. & Miao, J. (1998). *Acta Cryst.* A**54**, 232–239.
Shapiro, D., Thibault, P., Beetz, T., Elser, V., Howells, M., Jacobsen, C., Kirz, J., Lima, E., Miao, H., Neiman, A. M. & Sayre, D. (2005). *Proc. Natl. Acad. Sci. USA*, **102**, 15343–15346.
Toney, M. F., Samant, M. G., Borges, G. L., Blum, L. & Melroy, O. R. (1987). *J. Electrochem. Soc.* **134**, C508.
Tromp, R. M. (2000). *IBM J. Res. Dev.* **44**, 503–516.
Vartanyants, I. A., Pitney, J. A., Libbert, J. L. & Robinson, I. K. (1997). *Phys. Rev. B*, **55**, 13193–13202.
Vlieg, E., Vandergon, A. W. D., Vanderveen, J. F., Macdonald, J. E. & Norris, C. (1988). *Phys. Rev. Lett.* **61**, 2241–2244.
Walker, F. J., Specht, E. D. & Mckee, R. A. (1991). *Phys. Rev. Lett.* **67**, 2818–2821.
Warren, B. E. (1990). *X-ray Diffraction.* New York: Dover.
Williams, G. J., Pfeifer, M. A., Vartanyants, I. A. & Robinson, I. K. (2003). *Phys. Rev. Lett.* **90**, 175501.